Whole-Brain Imaging with Single-Cell Resolution Using Chemical Cocktails and Computational Analysis

Article *in* Cell · April 2014

Impact Factor: 32.24 · DOI: 10.1016/j.cell.2014.03.042 · Source: PubMed

16 authors, including:

Kazuki Tainaka
RIKEN
51 PUBLICATIONS **812** CITATIONS
SEE PROFILE

Dimitri Perrin
Queensland University of Technology
36 PUBLICATIONS **219** CITATIONS
SEE PROFILE

Hirotaka Onoe
RIKEN
186 PUBLICATIONS **2,414** CITATIONS
SEE PROFILE

Hideo Yokota
RIKEN
134 PUBLICATIONS **582** CITATIONS
SEE PROFILE

Please cite this article in press as: Susaki et al., Whole-Brain Imaging with Single-Cell Resolution Using Chemical Cocktails and Computational Analysis, Cell (2014), http://dx.doi.org/10.1016/j.cell.2014.03.042

Resource

Cell

Whole-Brain Imaging with Single-Cell Resolution Using Chemical Cocktails and Computational Analysis

Etsuo A. Susaki,[1,2,3,4,14] Kazuki Tainaka,[1,3,4,14] Dimitri Perrin,[2,14] Fumiaki Kishino,[5] Takehiro Tawara,[6] Tomonobu M. Watanabe,[7] Chihiro Yokoyama,[8] Hirotaka Onoe,[8] Megumi Eguchi,[9] Shun Yamaguchi,[9,10] Takaya Abe,[11] Hiroshi Kiyonari,[11] Yoshihiro Shimizu,[12] Atsushi Miyawaki,[13] Hideo Yokota,[6] and Hiroki R. Ueda[1,2,3,4,*]

[1]Laboratory for Synthetic Biology, RIKEN Quantitative Biology Center

[2]Laboratory for Systems Biology, RIKEN Center for Developmental Biology

2-2-3 Minatojima-minamimachi, Chuo-ku, Kobe, Hyogo 650-0047, Japan

[3]Department of Systems Pharmacology, Graduate School of Medicine, The University of Tokyo, 7-3-1 Hongo, Bunkyo-ku, Tokyo 113-0033, Japan

[4]CREST, Japan Science and Technology Agency, 4-1-8 Honcho, Kawaguchi, Saitama, 332-0012, Japan

[5]Faculty of Medicine, The University of Tokyo, 7-3-1 Hongo, Bunkyo-ku, Tokyo 113-0033, Japan

[6]Image Processing Research Team, RIKEN Center for Advanced Photonics, 2-1 Hirosawa, Wako, Saitama, 351-0198, Japan

[7]Laboratory for Comprehensive Bioimaging, RIKEN Quantitative Biology Center, OLABB, Osaka University, 6-2-3, Furuedai, Suita, Osaka 565-0874, Japan

[8]Bio-Function Imaging Team, RIKEN Center for Life Science Technologies, 6-7-3 Minatojima-minamimachi, Chuo-ku, Kobe City, Hyogo 650-0047, Japan

[9]Division of Morphological Neuroscience, Gifu University Graduate School of Medicine, 1-1 Yanagido, Gifu City, Gifu 501-1194, Japan

[10]PRESTO, Japan Science and Technology Agency, 4-1-8 Honcho, Kawaguchi, Saitama, 332-0012, Japan

[11]Laboratory for Animal Resources and Genetic Engineering, RIKEN Center for Developmental Biology, 2-2-3 Minatojima-minamimachi, Chuo-ku, Kobe, Hyogo 650-0047, Japan

[12]Laboratory for Cell-Free Protein Synthesis, RIKEN Quantitative Biology Center, 2-2-3 Minatojima-minamimachi, Chuo-ku, Kobe, Hyogo 650-0047, Japan

[13]Laboratory for Cell Function Dynamics, RIKEN Brain Science Institute, 2-1 Hirosawa, Wako, Saitama 351-0198, Japan

[14]Co-first author

*Correspondence: uedah-tky@umin.ac.jp

http://dx.doi.org/10.1016/j.cell.2014.03.042

SUMMARY

Systems-level identification and analysis of cellular circuits in the brain will require the development of whole-brain imaging with single-cell resolution. To this end, we performed comprehensive chemical screening to develop a whole-brain clearing and imaging method, termed CUBIC (*c*lear, *u*nobstructed *b*rain *i*maging *c*ocktails and *c*omputational analysis). CUBIC is a simple and efficient method involving the immersion of brain samples in chemical mixtures containing aminoalcohols, which enables rapid whole-brain imaging with single-photon excitation microscopy. CUBIC is applicable to multicolor imaging of fluorescent proteins or immunostained samples in adult brains and is scalable from a primate brain to subcellular structures. We also developed a whole-brain cell-nuclear counterstaining protocol and a computational image analysis pipeline that, together with CUBIC reagents, enable the visualization and quantification of neural activities induced by environmental stimulation. CUBIC enables time-course expression profiling of whole adult brains with single-cell resolution.

INTRODUCTION

Whole-brain imaging with single-cell resolution is one of the most important challenges in neuroscience, as it is required for system-level identification and analysis (Kitano, 2002) of cellular circuits in the brain. Various cross-sectional tomography methods have been developed to obtain high-resolution images throughout the brain (Gong et al., 2013; Li et al., 2010). Such section-based methods require expensive, specialized equipment, and the detailed structure between sections can be lost during sample processing. Alternatively, brain-transparentizing and -clearing techniques have been combined with rapid three-dimensional (3D) imaging using single-photon excitation microscopy, such as light-sheet fluorescence microscopy (LSFM) or specific plane illumination microscopy (SPIM). The 3D imaging can enable the study of systems from cells to organisms, such as cellular behavior in developing embryos and neural circuits in the adult brain (Dodt et al., 2007; Hägerling et al., 2013; Tomer et al., 2011). Such studies require a highly transparent sample for both illumination and detection.

Transparency is achieved by minimizing the light scattered by an object. Light is scattered at the boundary between materials with different refractive indices (RIs). Because lipids are a major source of light scattering in the fixed brain, the removal of lipids and/or adjustment of the RI difference between lipids and the surrounding areas are potential approaches for increasing brain

sample transparency. In an early trial of whole-brain imaging with macrozoom LSFM (Dodt et al., 2007), the brain tissue was cleared with BABB, a mixture of benzyl alcohol and benzyl benzoate. Because of BABB's hydrophobicity and because its high RI (1.56) (Becker et al., 2012) matched that of the fixed tissue, the sample was markedly cleared and suitable for observation with LSFM. Unfortunately, the clearing medium caused the rapid quenching of fluorescent signals. Although other organic chemical-based mixtures, such as tetrahydrofuran (THF) and dibenzyl ether (DBE) (Becker et al., 2012), performed somewhat better, some frequently used fluorescent proteins such as yellow fluorescent protein (YFP) were still quenched (Ertürk et al., 2012).

A hydrophilic chemical mixture called Sca*l*e was developed to clear brain samples (Hama et al., 2011). This urea-based reagent reduced quenching, and the resulting sample was suitable for both single-photon and multi-photon-based 3D tissue observation. Other issues, including relatively long sample treatment periods (weeks or months) and tissue swelling, were resolved by the development of another clearing reagent, SeeDB, which renders brain samples transparent within a few days by adjusting RI differences between the sample lipids and the surrounding tissue (Ke et al., 2013). SeeDB, a hydrophilic reagent lacking detergents or denaturation agents, preserves detailed structures as well as fluorescence signals. The remaining issue was that such simple hydrophilic reagents do not render whole-brain samples transparent enough for single-photon-based rapid whole-brain imaging. CLARITY, a recently reported technique for brain clearing (Chung et al., 2013), rendered brain samples transparent by aggressively removing lipids using electrophoresis. The resulting sample was highly transparent and suitable for LSFM imaging; however, use of a specialized electrophoresis device with a narrow range of optimal parameters makes parallelization and comparison among different samples difficult. Thus, although previous protocols have addressed some of the issues required for the efficient clearance of brain samples, an improved protocol was still required for whole-brain imaging with single-cell resolution.

The anatomical annotation of images is also critical. In conventional human brain imaging techniques such as computed tomography (CT) (Cormack, 1973), magnetic resonance imaging (MRI) (Lauterbur, 1973), and functional magnetic resonance imaging (fMRI) (Ogawa et al., 1990), anatomical annotation consists of two steps: (1) acquisition of whole-brain structural and specific signal (or functional) images and (2) computational analysis of these images. For example, fMRI, which visualizes neural activity, is almost always accompanied by MRI, which acquires a structural image of the whole brain. This image is then used for image registration and alignment to a standard whole-brain image ("reference brain") so that signal images can be compared across individuals. Because computational image analysis is so essential, informatics tools have been developed and implemented to facilitate this process in conventional human brain imaging (Avants et al., 2011). However, this kind of computational image analysis is rare for fluorescence imaging of whole mammalian brains due to the lack of whole-tissue histological counterstaining of cell nuclei, which can be used for anatomical orientation. 3D images acquired with sectional tomography or tissue-clearing protocols provide information on fluorescently labeled cells, but not on the overall shape and characteristic anatomical structures that are required for the registration and alignment steps. Even in a trial in which the image registration step was successful, manual determination of landmark structures was necessary (Gong et al., 2013). The larger number of images generated in time-course experiments makes the need for automated processing even more acute. Thus, efficient anatomical annotation will be required for whole-brain imaging with single-cell resolution.

We have developed a simple, efficient, and scalable brain-clearing method and computational analysis pipeline, CUBIC (*c*lear, *u*nobstructed *b*rain *i*maging *c*ocktails and *c*omputational analysis), that enables rapid whole-brain imaging with single-photon excitation microscopy. CUBIC can be applied to whole-brain imaging of various fluorescent proteins and 3D imaging of immunostained adult brain samples. CUBIC is scalable from primate brain imaging to subcellular structures such as axons and dendritic spines. In order to facilitate interindividual comparisons, we have also developed an anatomical annotation method using a whole-brain cell-nuclear counterstaining protocol and a computational image analysis pipeline. CUBIC enables the time-course expression profiling of adult whole brains with single-cell resolution.

RESULTS

Development of CUBIC Reagents by Comprehensive Chemical Screening

To develop a simple, efficient, and scalable tissue-clearing protocol for whole-brain imaging, we started by rescreening the chemical components of the hydrophilic brain-clearing solution Sca*l*eA2 (Hama et al., 2011). We started with this protocol because of its ease and its ability to preserve fluorescent signals. We considered 40 chemicals, including polyhydric alcohols, detergents, and hydrophilic small molecules (Table S1 available online), corresponding to the components of the Sca*l*eA2 solution: glycerol, Triton X-100, and urea. To evaluate the clearing efficiency of these chemicals, we first sought to improve the experimental throughput of clearing measurements. In a typical evaluation procedure, we first fix, isolate, and immerse a whole mouse brain in one chemical mixture and then evaluate the clearing efficiency of the chemical by measuring the transmittance of the fixed, cleared whole brain. For a more efficient evaluation protocol, we exchanged the order of the fixation and isolation steps and introduced a homogenization step so that many chemicals can be tested using only one mouse brain (Figure 1A and Extended Experimental Procedures). This "solubilization" assay using a homogenized suspension instead of a whole brain enabled the reproducible, quantitative, and comprehensive evaluation of chemicals for their ability to dissolve brain tissue (Figure 1B). We also evaluated the quenching effect of each chemical on EGFP fluorescence in this first chemical screening (Figure 1C). We noted that a series of aminoalcohols (#4, #8, #9, #10, #15, #16, #17) showed considerable brain tissue solubilizing activity, whereas polyhydric alcohols without amino groups (#1, #2, #3, #5, #12, #18, #19, #20) exhibited much less activity (Figure 1B and Table

S1). This may indicate that the cationic amino group contributes to solvating anionic phospholipids, the most abundant lipids in the brain. In addition, basic aminoalcohols preserved and even enhanced EGFP fluorescent signals, whereas some weakly acidic amine-free alcohols (#1, #2, #3, #11) quenched the fluorescence (Figure 1C and Table S1). Many fluorescent proteins, such as EGFP, EYFP, and mCherry, contain a phenolate chromophore, which is highly pH sensitive, resulting in increased fluorescence intensity with increasing pH (until the protein denatures) (Kneen et al., 1998). In a highly concentrated aqueous medium without buffers, basic aminoalcohols were therefore more suitable clearing agents than other weakly acidic or neutral alcohols. After a second chemical screening (Figures 1D and 1E), our cocktail finally included *N,N,N′,N′*-tetrakis(2-hydroxypropyl) ethylenediamine (#10), Triton X-100 (#25), and urea (#36) (Figure S1B). We refer to this first CUBIC reagent as Sca*l*eCUBIC-1 (hereafter denoted as reagent 1). We used the words "Sca*l*e" and "CUBIC" because this reagent is based on urea (Sca*l*e) and aminoalcohols (CUBIC), respectively.

Reagent 1 treatment of the whole adult mouse brain resulted in a highly transparent brain (Figures 2A and 2B). The lipid-rich white matter was not completely cleared, possibly due to incomplete lipid removal and unmatched RIs between the tissue and solution. Sca*l*eCUBIC-2 (hereafter denoted as reagent 2) was developed by modifying the reagent 1 recipe in a third chemical screening (Figure S1A). Addition of a high concentration of sucrose instead of glycerol increased the reagent RI (from 1.45-1.46 for glycerol-based reagent 2 to 1.48–1.49 for sucrose-based reagent 2, which is similar to the RI of SeeDB [RI = 1.49] [Ke et al., 2013]) so that it matched the tissue RI and increased the transmittance (Figure S1A). Replacing chemical #10 with 2,2′,2′′-nitrilotriethanol (#16) also reproducibly increased the transmittance (Figure S1A), motivating its inclusion in the final version of reagent 2 (Figures 2A and S1B). As expected, reagent 2 enhanced the optical clearance of lipid-rich regions deeper in the brain (Figure 2A).

CUBIC Is a Simple and Efficient Procedure

As summarized in Figure 2A, the CUBIC protocol involves a series of immersion steps followed by a washing step. The CUBIC brain samples were sufficiently transparent for adult whole-brain imaging. The sample was slightly swollen by reagent 1 treatment but returned to its original size following reagent 2 treatment. In addition, CUBIC-based clearing can be used to clear an acrylamide gel-embedded sample prepared according to the CLARITY protocol (Chung et al., 2013), addressing concerns about destruction of detailed anatomical structures and protein loss (Figure S1C).

Sample clearing with CUBIC reagents required 2 weeks for completion, comparable to CLARITY (~10 days) (Chung et al., 2013) and faster than Sca*l*eA2 (weeks) and Sca*l*eU2 (months) (Hama et al., 2011). Although clearing with 3DISCO can be completed in 5 days, fluorescence signals are quenched within a few days of preparation (Ertürk et al., 2012). To evaluate the quenching effect of CUBIC, we next incubated various recombinant fluorescent proteins with reagent 1, reagent 2, or PBS for 24 hr or 7 days (Figure 2C). The fluorescence of all of the tested proteins, even EYFP, the most sensitive, remained high after the 7-day incubation. The CUBIC protocol achieved comparable transparency to other recently developed methods in a reasonable time, with minimal quenching of fluorescence signals. Notably, the red fluorescent proteins mCherry and mKate2 also showed minimal quenching. Given that red light transmits through tissues more efficiently than shorter wavelength light (Figure 2B), these proteins are very suitable as labeling tools for use with the CUBIC protocol.

To confirm that CUBIC samples can be used for deep brain imaging, we performed two-photon imaging of a Thy1-YFP-H Transgenic (Tg) mouse brain (Feng et al., 2000) with an objective lens optimized for use with SCALEVIEW-A2 (working distance 8 mm, optimized for RI = 1.38) (Figure 2D). We treated a hemisphere with reagent 1 for 3 days and acquired a Z stack image. Treatment with reagent 1 alone was sufficient for deep brain imaging (up to ~4 mm) with two-photon excitation microscopy (Figure 2D). The accelerated clearing obtained with reagent 1 enabled substantially deep brain imaging up to ~4 mm, whereas SCALEVIEW-A2-treated samples became transparent more slowly (Figure S2).

CUBIC Enables Rapid, High-Performance, Whole-Brain Imaging with LSFM

The high transparency of CUBIC samples and the two-photon imaging results prompted us to perform whole-brain imaging with single-photon excitation microscopy techniques such as LSFM. Previous reports have used confocal- or multi-photon-based imaging methods (Chung et al., 2013; Ke et al., 2013), in which image tiling and data acquisition time (days for a single brain) were significant challenges. LSFM, which enables rapid whole-brain imaging, was used in a previous study using BABB (Dodt et al., 2007), though fluorescence signal loss over time was a problem. We first set up an optimized macro-zoom microscope combined with a light-sheet illuminator (LaVision Ultramicroscope) (Figure S3A) so that an entire horizontal section of a mouse brain can be acquired in a single plane with subcellular resolution (theoretical X-Y resolution in the acquired image is 4.7 μm). For rapid whole-brain imaging, we generated a knockin mouse strain expressing three tandem repeats of *mKate2* with a nuclear localization signal, under control of the CAG promoter (Niwa et al., 1991) from the ROSA26 locus. We used mKate2 because of its signal intensity, photostability, and rapid protein maturation (Chudakov et al., 2010), as well as its resistance to fluorescence quenching by CUBIC reagents (Figure 2C).

We then collected Z stack images of the horizontal section (Movie S1) of a CUBIC whole brain from two directions (dorsal to ventral, D-V, and ventral to dorsal, V-D). With our current microscope setup, imaging took 30 min to 1 hr per brain/color/direction. The reconstituted 3D whole-brain image of the mKate2 knockin mouse (Figures 3A and S3B) and its virtual coronal sections (Figure 3B) enabled the 3D visualization of spatial gene expression patterns and the examination of detailed internal structures. Furthermore, we confirmed that background fluorescence in CUBIC samples is low enough not to impair visualization of the fluorescent signal from mKate2 in the overall brain image data (Figures 3F–3I and Extended Experimental Procedures).

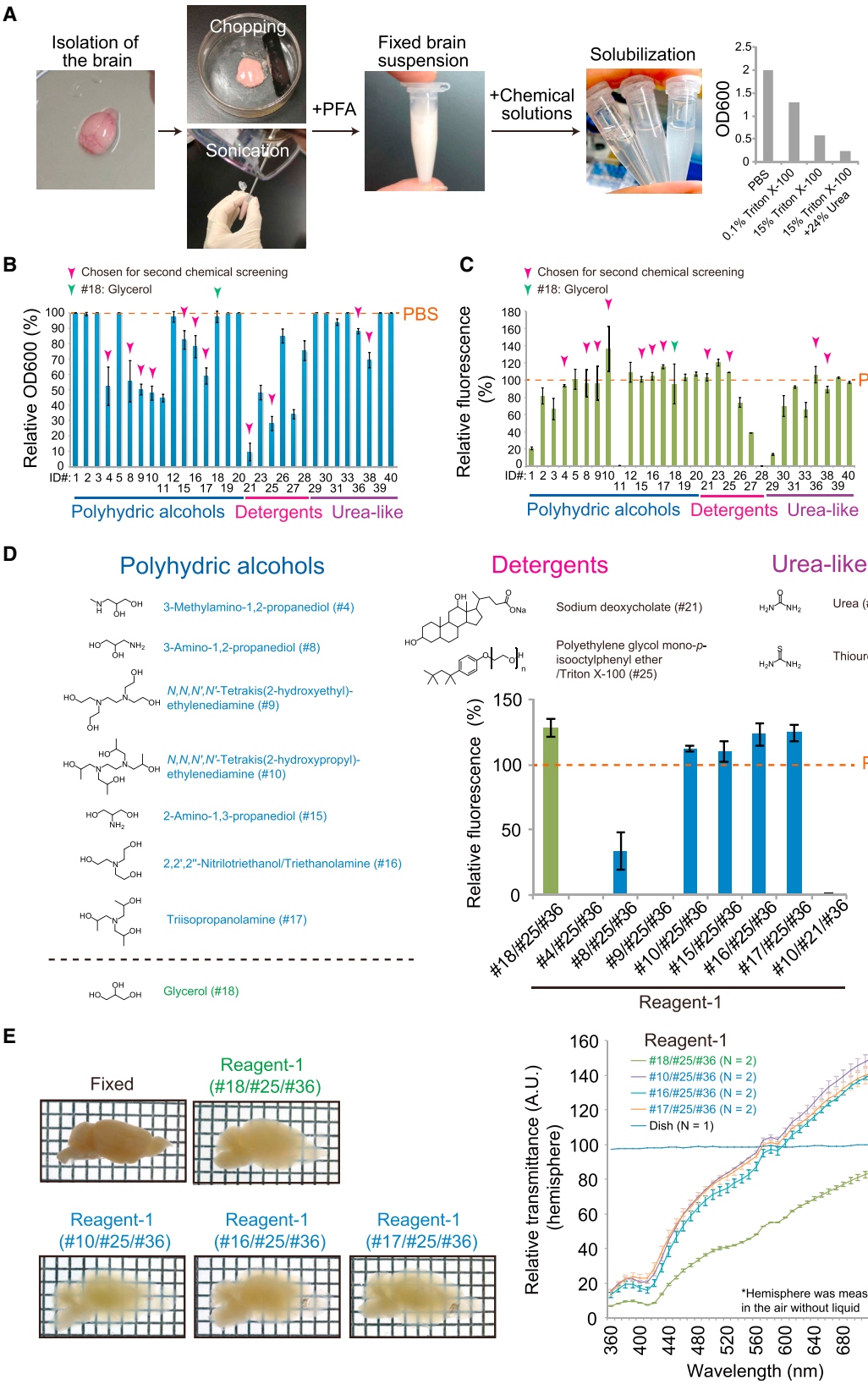

(legend on next page)

CUBIC Is Applicable to the Whole-Brain Imaging of Various Fluorescent Proteins

Our successful imaging using mKate2 led us to test other fluorescent proteins, including mCherry, EGFP, and YFP. We performed similar whole-brain imaging with CUBIC adult whole brains from three mouse strains: an mCherry-fused histone-2B-expressing strain (R26-H2B-mCherry [CDB0239K]; Figures 3C and S3C; Abe et al., 2011), an EGFP-fused histone-2B-expressing strain (R26-H2B-EGFP [CDB0238K]; Figures 3D and S3D; Abe et al., 2011), and a Thy1-YFP-H transgenic strain (Figures 3E and S3E). By comparing the reconstituted sections of these samples, spatial gene expression patterns and their differences across samples could be easily traced. For example, we compared two knockin strains in which the gene was inserted into the same ROSA26 locus but regulated by different promoters; the gene for mKate2 was regulated by the CAG promoter and, for mCherry, by the endogenous ROSA26 promoter. The whole-brain image showed expression differences in regions such as the thalamus, hypothalamus, midbrain, granular layer of the cerebellum, and ventricular choroid plexus (Figures S3F and S3G). These results show that various fluorescent proteins can be used for rapid and high-performance whole-brain imaging with the CUBIC protocol.

CUBIC Is Applicable to Adult Brain Imaging of 3D-Immunostained Samples

Given that CUBIC samples were highly permeabilized by lipid removal, we predicted that the CUBIC protocol would be useful for the immunostaining of large blocks of brain tissue, a potential improvement over sectional staining. We performed 3D immunohistochemistry (3D-IHC) using a brain block containing the hypothalamus region (Figure 4A). The block was subjected to reagent 1 treatment, followed by 3D-IHC with antibodies to neuropeptides expressed in the suprachiasmatic nucleus (SCN), the central clock of the mammalian circadian system. We used antibodies for Copeptin (a peptide cleaved from the common precursor of arginine vasopressin [AVP]; Land et al., 1982) and for vasoactive intestinal peptide (VIP) to label the AVP and VIP neurons in the nucleus. After immunostaining, the block was treated with reagent 2 for further clearing, and the resulting sample was observed with an inverted single-photon confocal microscope. We imaged a horizontal plane of the SCN and paraventricular nucleus (PVN) regions of the hypothalamus from the bottom of the brain. The immunostained signals were detected at a depth of >750 μm (from the bottom of the brain to the dorsal area of the PVN in the hypothalamus) and were visualized as a 3D reconstituted image (Figure 4B and Movie S2). In the acquired horizontal images, the cell bodies and fibers of the two types of neurons were clearly visible (Figure 4C). High-resolution images were also included (Figure S4C). Abrahamson and Moore have demonstrated that a large number of VIP-positive soma were densely packed in the ventral area of the SCN and that AVP-positive soma were localized in the dorsomedial and ventrolateral area of the SCN and dorsally distributed even around the paraventricular nucleus (Abrahamson and Moore, 2001). The ventral image at a depth of ~45 μm (including the most ventral area of the SCN) displayed extensive VIP-positive soma signals in the left panel of Figure S4C. The middle image at a depth of ~65 μm (including the more dorsal area of the SCN) exhibited AVP-positive soma and VIP-positive fibers in the middle panel of Figure S4C. The dorsal image at a depth of ~780 μm (including the paraventricular nucleus) included sparse AVP-positive soma in the right panel of Figure S4C. Therefore, previously reported spatial distributions of AVP- and VIP-positive soma and fibers were clearly recapitulated by CUBIC-based 3D IHC.

We further applied 3D-IHC analysis to the SCN of both wild-type (WT) and a *Cry1*$^{-/-}$, *Cry2*$^{-/-}$ clock gene double-knockout strain (van der Horst et al., 1999), sacrificed at different circadian times (CT). For these samples, nuclear counterstaining with SYTO 16, a cell-permeable green fluorescent nucleic acid stain, was performed during the reagent 1 treatment. Plane images at different depths (Figures 4D and S4A) and reconstituted 3D images (Movies S3 and S4) showed CT-dependent differences in the staining patterns of these two neuropeptides. The most striking difference was that the fibers in the dorsal region of the SCN were more strongly stained at CT0 than at other circadian times. This tendency was reproduced in an independent set of

Figure 1. Development of CUBIC Reagents by Comprehensive Chemical Screening

(A) Method for screening chemicals for brain-solubilizing activity using a fixed brain suspension. Turbidity of the suspension was quantitatively determined with an absorptiometer and was expressed as an OD600 value. See also Extended Experimental Procedures and Table S1.

(B) Solubilization assay. The fixed brain suspension was mixed and incubated with 10 wt% aqueous solutions of candidate chemicals. After 24 hr, the mixtures were subjected to OD600 measurement.

(C) EGFP quenching assay. Recombinant EGFP was incubated in 10 wt% aqueous solutions of candidate chemicals for 12 hr, after which the fluorescence signals were measured.

In (B) and (C), the data represent the average (±SD) of two independent measurements. Chemicals without ID number were rejected before the step due to their low solubility (<10 wt%) or unavailability (see Table S1). Chemicals chosen for the second chemical screening in (D) and glycerol (#18) are indicated with magenta arrowheads and a green arrowhead, respectively.

(D) Second chemical screening of candidate chemicals for reagent 1. The EGFP quenching assay was performed with the final recipe of reagent 1 (Figure S1B). Fluorescent signal intensities were measured as in (C), and the average relative fluorescence ± SD of two independent measurements is shown in the graph. #38 was rejected due to its relatively low solubility (<15 wt% in water).

(E) Effect of using aminoalcohols instead of glycerol in reagent 1. From the results in (D), we chose aminoalcohols (#10, #16, #17), Triton X-100 (#25), and urea (#36) for further evaluation. Glycerol (#18) was also tested as a Sca*l*e-based mixture, as in (D). #15 was rejected due to its cost and safety concerns (see Table S1). Fixed mouse hemispheres were subjected to clearing with the indicated solutions for 3 days followed by measurement of transmittance (360–740 nm). The transmittance data are shown as relative transmittance, normalized to the blank, defined as 100. The values in the graph represent the average ± SEM from two independent samples. Note that some of the values exceeded 100, possibly due to the difference in the RI of the sample and the surrounding air (see Extended Experimental Procedures).

See also Figure S1.

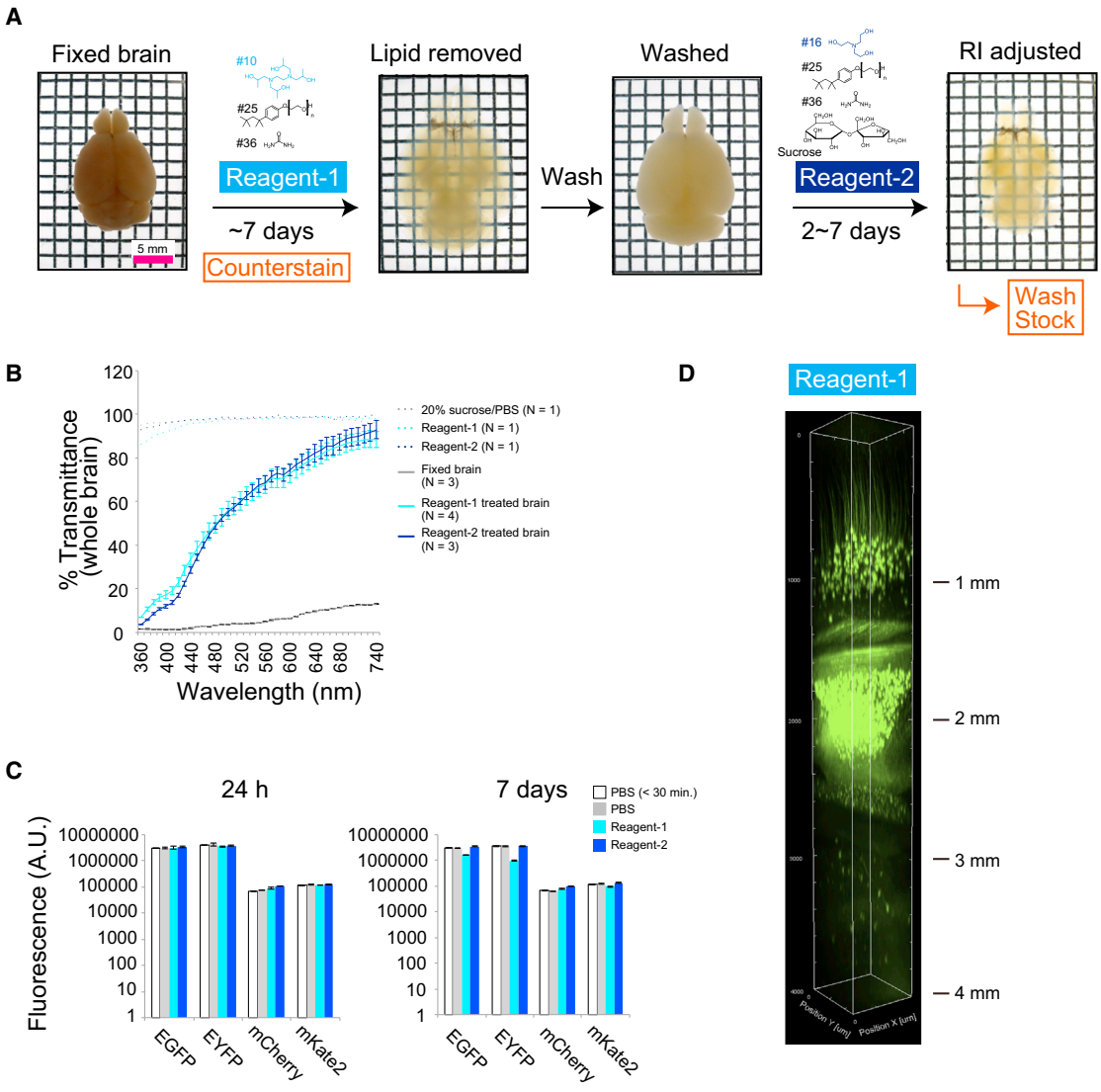

Figure 2. CUBIC, A Simple and Efficient Whole-Brain Clearing Protocol

(A) CUBIC protocol. A fixed whole brain (from a 6-month-old mouse) was treated with reagent 1 to remove lipid components for up to 7 days, followed by washing with PBS. The sample was then treated with reagent 2 for 2–7 days to adjust the refractive indices of the tissue and reagent. Optional procedures are indicated in orange boxes: nuclear counterstaining during reagent 1 treatment, and sample storage at 4°C or –80°C after completion.

(B) Transmission curves. Light transmittance (360–740 nm) of fixed whole brain (n = 3), reagent-1-treated whole brain (day 7, n = 4), reagent-2-treated whole brain (day 3, n = 3), and the corresponding reagents (n = 1, for each reagent) were measured and normalized to the blank. Data shown represent the average ± SEM.

(C) Quenching test of fluorescent proteins by CUBIC reagents. The indicated recombinant fluorescent proteins were incubated in each reagent or PBS for 24 hr or 7 days, followed by measurement of the fluorescent signal intensity. Data shown represent the average ± SD of three independent measurements.

(D) Two-photon deep brain imaging of a reagent-1-treated Thy1-YFP-H Tg hemisphere. A single hemisphere was treated with the reagent 1 for 3 days at 37°C. The resulting sample was observed using two-photon microscopy.

See also Figure S2.

experiments (Figure S4A) as well as in animals housed under light-dark conditions (Figure S4B). These differences were not observed in images of the *Cry1*$^{-/-}$, *Cry2*$^{-/-}$ strain captured at CT0 and CT12 (Figures 4D and S4A), suggesting that the observed immunostaining differences in the AVP and VIP neurons were dependent on the circadian clock. The CUBIC protocol is highly applicable to the 3D imaging of immunostained adult-brain blocks.

CUBIC Is Scalable from Subcellular Structures to a Primate Brain

In addition to the efficiency of the CUBIC protocol, its scalability is also important for a wide range of applications. One potential application of a brain-clearing protocol is to trace neural connections at the axon or synapse level. We therefore tested whether detailed cell structures such as axons and spines were preserved in CUBIC samples. We used Thy1-YFP-H transgenic

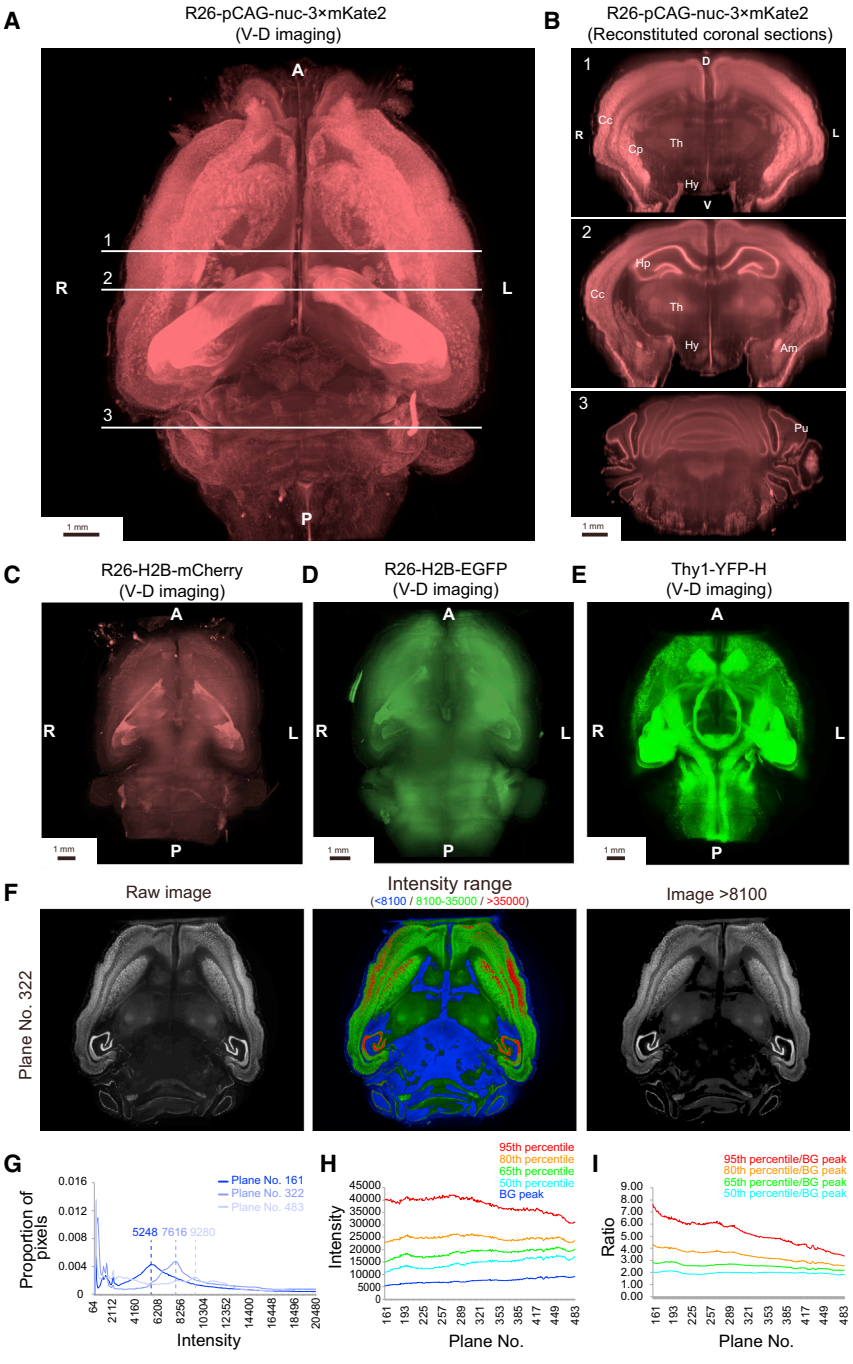

Figure 3. CUBIC Can Be Used for Rapid and High-Performance Whole-Brain Imaging of Various Fluorescent Proteins

3D-reconstituted images of mouse brains expressing various fluorescent proteins were acquired with LSFM. A, anterior; P, posterior; R, right; L, left; D, dorsal; V, ventral. Ventral view is shown.

(A) R26-pCAG-nuc-3 × mKate2 mouse brain (5-week-old mouse). Images were acquired from the ventral-to-dorsal (V-D) direction. Z stack: 10 μm step × 646 planes, with 0.28 s × two illuminations.

(B) Reconstituted coronal sections at the indicated positions (1–3) shown in (A). Cc, cerebral cortex; Cp, caudoputamen; Th, thalamus; Hy, hypothalamus; Hp, hippocampus; Am, amygdala; Pu, Purkinje cell layer.

(C) V-D image of a R26-H2B-mCherry mouse brain (6-month-old mouse). Z stack: 10 μm step × 709 planes, with 4 s × two illuminations.

(D) V-D image of a R26-H2B-EGFP mouse brain (6-month-old mouse). Z stack: 10 μm step × 665 planes, with 4 s × two illuminations.

(E) V-D image of a Thy1-YFP-H Tg mouse brain (2-month-old mouse). Z stack: 10 μm step × 696 planes, with 0.3 s × two illuminations. See also Figure S3 and Movie S1.

(F) (Left) Raw TIFF image from plane 322 of the R26-pCAG-nuc-3 × mKate2 mouse brain. (Center) False-color image highlighting regions with intensity <8,100 (blue), between 8,100 and 35,000 (green), and >35,000 (red). In each channel, brighter colors mean higher intensity within the range in the raw image. (Right) Processed image for plane 322, where all pixels whose intensity is below 8,100 are set to black.

(G) Low-intensity peaks (corresponding to background peaks) in the TIFF image histogram, shown for planes 161, 322, and 483.

(H) Background peaks (BG peak) and percentiles for the intensity distribution of pixels whose intensity is at least 5% higher than BG peak.

(I) Ratios between the percentiles and the background peaks shown in (H).

mice in which neuronal subcellular structures, including somata, axons, and dendritic spines, can be labeled and visualized by YFP fluorescence (Feng et al., 2000). A magnified view of a CUBIC brain sample from the Thy1-YFP-H transgenic mouse revealed that the axons and somata of neurons were well preserved (the pontine-medullary region in the LSFM image is shown in Figure S5A). A single axon was labeled and visualized without any breaks, making its trajectory easily traceable. In addition, the dendritic spines in the cerebral cortex of the same strain were clearly observed by two-photon microscopy (Figure S5B). Furthermore, proteins in the spine were also preserved in the CUBIC sample by immunostaining with an antibody against synapsin I, a phosphoprotein associated with synaptic vesicles in neural synapses (Navone et al., 1984) (Figure S5C). Synaptic proteins were preserved in the CUBIC samples, suggesting that CUBIC is scalable to subcellular structure imaging.

Another potential application for a brain-clearing protocol is in primate whole-brain imaging. The marmoset is becoming an increasingly popular primate model organism in neuroscience because of its potential for genetic engineering (Sasaki et al., 2009). We tested whether the CUBIC protocol is applicable to marmoset whole-brain fluorescence imaging with nuclear counterstaining. A postnatal-day-3 marmoset brain has ~10 times the volume of an adult mouse brain (Figure 5A). CUBIC treatment

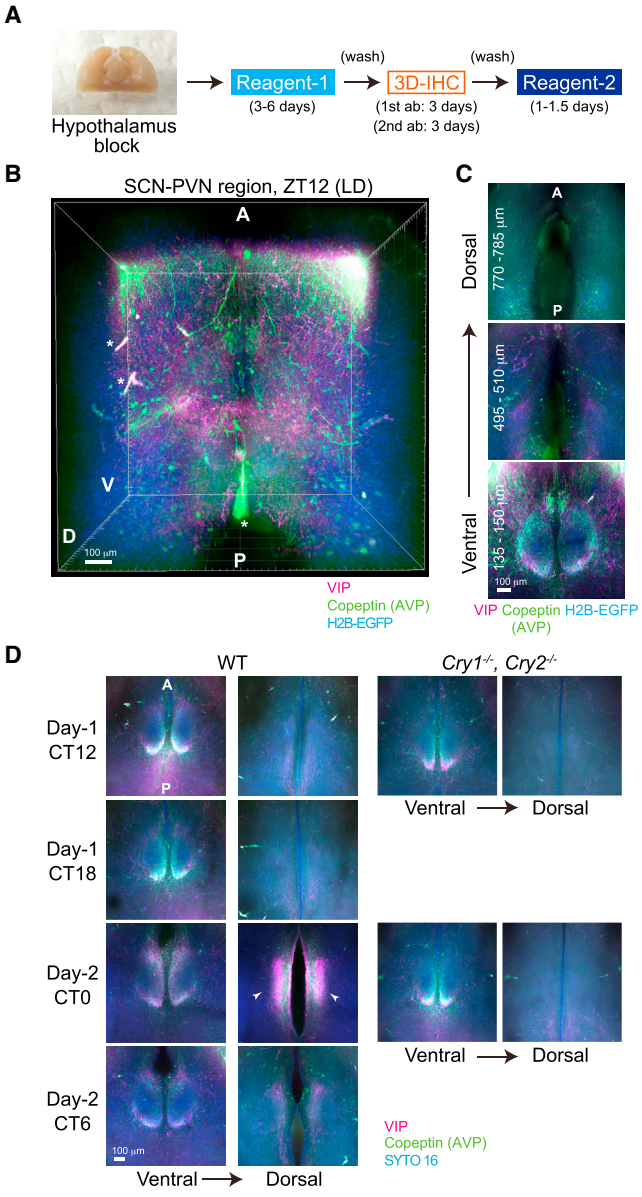

Figure 4. CUBIC Can Be Used for Imaging of 3D Immunostained Adult Brain Samples

(A) CUBIC treatment procedure and 3D immunohistochemistry (3D-IHC) of a hypothalamus block with anti-VIP and -Copeptin antibodies (1st ab) and Alexa-conjugated second antibodies (2nd ab).

(B) 3D view of the SCN region of R26-H2B-EGFP mouse. Sampling was performed at zeitgeber time 12 (ZT12) under 12 hr:12 hr light-dark conditions. Horizontal images were acquired from the ventral side with an inverted confocal microscope (Z stack: 4.99 μm step × 173 planes). A, anterior side; P, posterior side; D, dorsal side; V, ventral side. Asterisks indicate nonspecific signals in the third ventricle and the vessels.

(C) Selected horizontal images (Z projection with maximum intensity, 4.99 μm step × 3 planes) from (B). Approximate depth from the first image of the Z stack data are indicated.

(D) 3D-IHC results of the WT and *Cry1*$^{-/-}$, *Cry2*$^{-/-}$ SCN, collected at different time points under constant dark conditions. Nuclear counterstaining with SYTO 16 was performed during reagent 1 treatment. Depth of the horizontal images was ~140 μm on the ventral side and 290 μm on the dorsal side (Z projection with maximum intensity, 1.98 μm step × 3 planes) from the most ventral plane of the SCN region. Strong signals for the neuropeptides were detected on the dorsal side of the WT SCN at CT0 of day 2 (arrowheads), which were barely detected in the *Cry1*$^{-/-}$, *Cry2*$^{-/-}$ SCN. Images were acquired and processed in a similar but optimized condition for each sample so that most of the stained signals were obtained in the unsaturated range of intensity.

See also Figure S4 and Movies S2–S4.

with SYTO 16 staining of the hemisphere from a 3-day-old marmoset resulted in clearing comparable to that achieved with the mouse brain (a hemisphere was used instead of a whole marmoset brain due to the size limitation of the microscope stage used in this study; Figure 5B). The acquired raw images were subjected to 3D image reconstitution to generate a volume-rendering image (Figures 5C and 5D) and reconstituted sections (Figure 5E). The reconstituted image clearly depicts general and detailed structures of the marmoset brain, such as vessels and layers of the cerebral cortex (Figures 5C–5E and Movie S5). These results suggest that the CUBIC protocol is scalable to larger tissues, indicating its potential application to various animals, including primates. Together, the CUBIC protocol is scalable from subcellular structures to a primate brain, a feature that will support wide-ranging applications in neuroscience.

Whole-Brain Nuclear Counterstaining and Computational Image Analysis in CUBIC Enable the Visualization of Neural Activities Induced by Environmental Stimulation with Single-Cell Resolution

Another challenge for establishing whole-brain imaging with single-cell resolution is the development of anatomical annotation. For this purpose, we used Arc-dVenus transgenic mice, in which an unstable Venus protein is expressed under the control of a neural activation marker gene, *Arc* (Eguchi and Yamaguchi, 2009). Arc-dVenus transgenic mice were housed under constant dark conditions for about 2.5 days and were then exposed to constant light at CT2.5, followed by fixation and collection of their brains (Figure 6A). As previously reported, light-dependent neural activation was observed with fluorescent stereomicroscopy, showing increased Venus signals in the visual area of the cortex in a light-exposed brain (Figure S6A, Light+ (1)), compared with a control brain (Figure S6A, Light−).

Because anatomical annotation requires the acquisition of whole-brain structural images, we performed nuclear counterstaining with propidium iodide (PI) to acquire whole-brain structural images in the red channel. The brain samples were subjected to CUBIC treatment with PI counterstaining, and the resulting samples were analyzed by whole-brain imaging with LSFM. The reconstituted 3D images clearly revealed light-responsive neurons, such as those in the visual area (Vi) (Figures 6B and 6C and Movies S6 and S7). Individual neurons were clearly visible, suggesting that the whole-brain image achieved single-cell resolution. Several additional brain regions, including the orbital area (Or), the motor area (Mo), the anterior cingulate area (Ac), the orbital area, and subcortical areas in the forebrain (such as the claustrum and endopiriform nucleus [Cl/Ep]), also exhibited increased Venus signals in the light-exposed brain (Figure 6B), compared to the control brain (Figure 6C). These areas are known

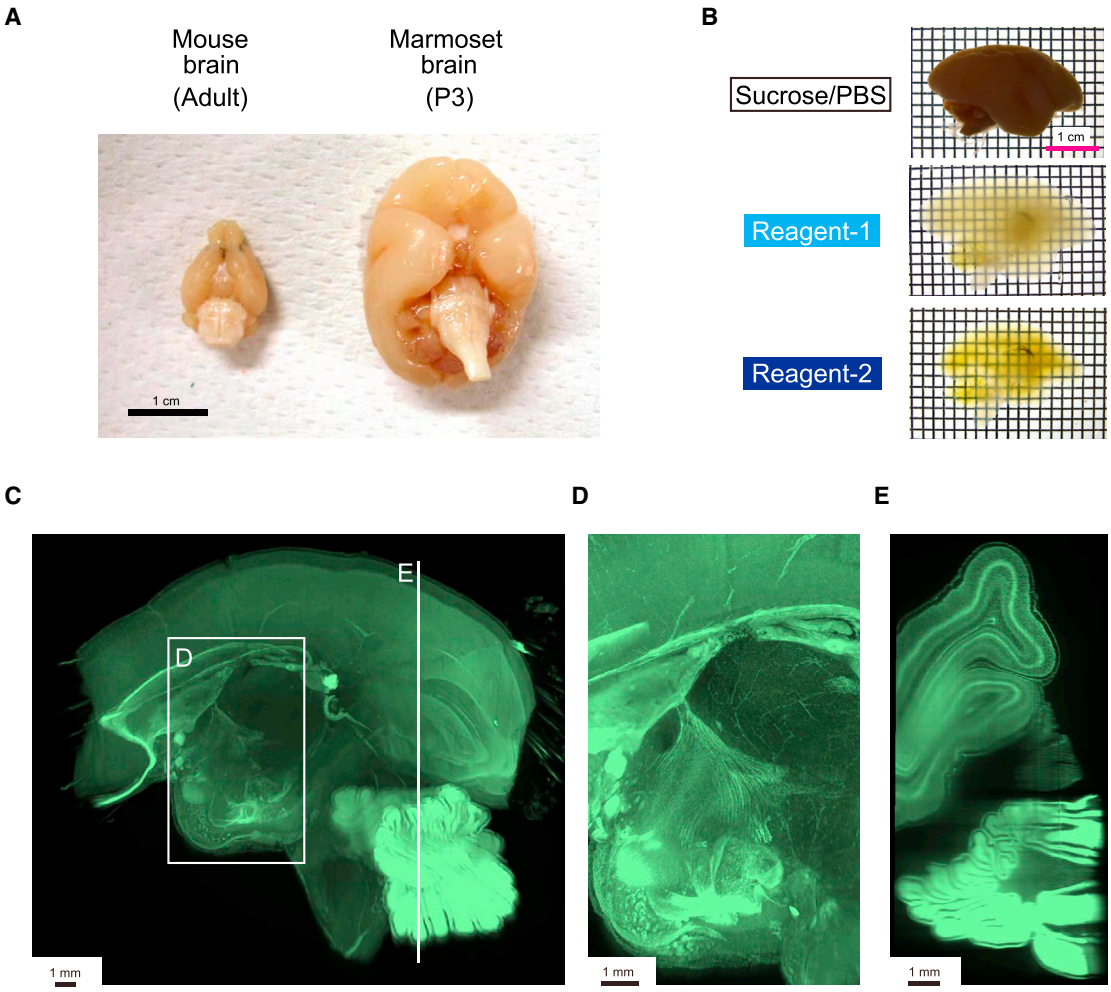

Figure 5. CUBIC Is Scalable to a Primate Brain

(A) Comparison of the size of an adult mouse brain and a postnatal day 3 (P3) marmoset brain.

(B) CUBIC treatment and SYTO 16 nuclear staining of the marmoset hemisphere. The images of the same marmoset hemisphere after reagent 1 and reagent 2 treatments are shown.

(C–E) A 3D-reconstituted fluorescent image of the nuclear-stained marmoset hemisphere (Z stack: 10 μm step × 900 planes, with 0.25 s × two illuminations) acquired with LSFM. Magnified view of the boxed region in (C) is shown in (D). A reconstituted coronal section at the indicated position in (C) is shown in (E). Anatomical structures such as vessels and layers of the cerebral cortex can be observed in the reconstituted images.

See also Figure S5 and Movie S5.

to be connected to each other and to respond to several sensory stimuli (Miller and Vogt, 1984; Reep et al., 1996; Sloniewski et al., 1986). This result was reproduced in another light-exposed brain (Light+ (2) in Figures S6A and S6B).

We next focused on the development of a computational image analysis pipeline ("CUBIC informatics," Figure 7A). We first combined whole-brain images of the same brain that had been captured from two opposite directions (dorsal-to-ventral [D-V] and ventral-to-dorsal [V-D]) (Figures S7A and S7B). This was necessary because whole-brain images captured from the dorsal-to-ventral direction (D-V images) were clear on the dorsal side but blurred on the ventral side and vice versa (Figures S7C and S7E, V-D image and D-V image). To combine the two images, we first aligned them (Figure S7A) and then generated a single whole-brain image by considering the sharpness of each horizontal plane (Figure S7D). The blurred areas were compensated for in the combined image (Figure S7E, combined image), which was used for subsequent computational analysis.

Applying this pipeline to Arc-dVenus transgenic mouse brains, we aligned the combined PI image of an internal reference brain (Light−) to a reference brain (Figure 7B), aligned the PI images captured from the Light+ and Light− brains (Figure 7C), and directly compared the dVenus fluorescence signals of these brains by overlaying their aligned images (Figure 7D). Subtraction of the signal intensities clearly showed the brain regions stimulated by light (Figure 7E). These regions included areas identified in Figures 6B and S6B but with improved clarity due

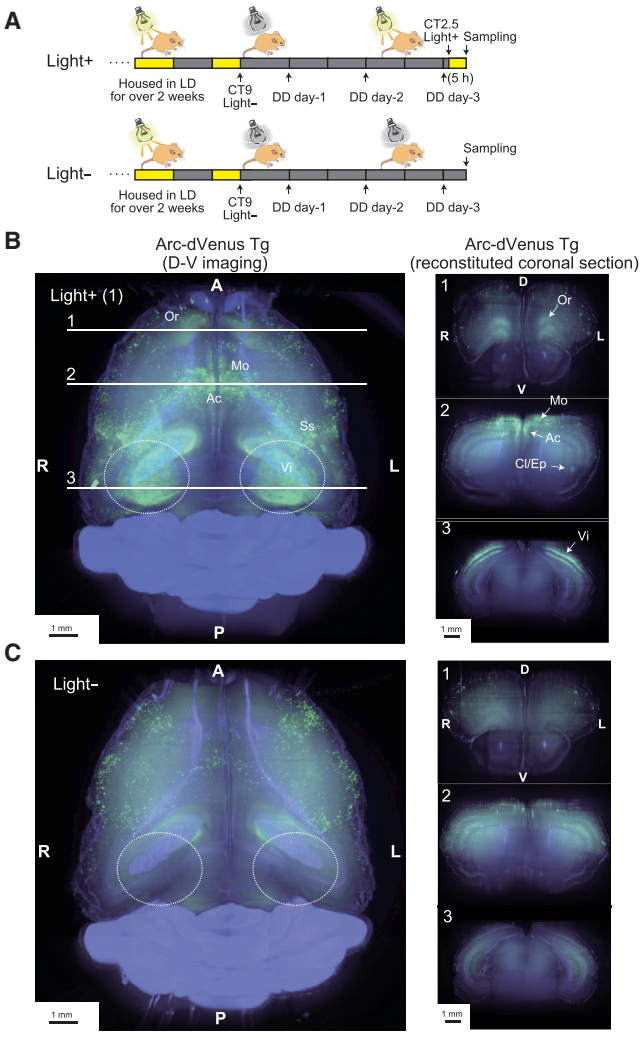

Figure 6. Whole-Brain Nuclear Counterstaining in CUBIC Enables the Visualization of Neural Activities Induced by Environmental Stimulation

(A) Experimental scheme. Arc-dVenus Tg mice (11 weeks old) housed under constant dark (DD) conditions for about 2.5 days were then stimulated by light (Light+) or maintained in the dark (Light−) and were sacrificed 5 hr after stimulation.

(B and C) Whole-brain images and reconstituted coronal sections (indicated positions in the whole brain image in (B) of CUBIC brains from Light+ (1) and Light− mice, corresponding to Figure S6A. The brains were stained with PI (light purple), and two-color D-V images were acquired with LSFM (Z stack: 10 μm step × 625 planes for B and 10 μm step × 648 planes for C, with 3 s × two illuminations for Venus and with 0.3 s × two illuminations for PI, respectively). A region including the visual area is indicated by the dotted ellipse. Areas where Venus signals were increased in the Light+ brain are indicated in the whole-brain image and reconstituted coronal sections in (B).

Or, orbital area; Mo, motor area; Ac, anterior cingulate area; Ep, endopiriform nucleus; Cl, claustrum; Vi, visual area; Ss, somatosensory area. See also Figure S6 and Movies S6 and S7.

to the sharper combined image. The CUBIC protocol combined with CUBIC informatics enables gene expression profiling of adult whole brains.

DISCUSSION

CUBIC Is a Simple, Efficient, and Scalable Protocol of Wide Applicability

The CUBIC protocol appears to have reconciled some of the seemingly incompatible demands of previous methods. First, it is simple in that it requires only the immersion of tissue in two reagents for relatively short periods (Figure 2). Simplicity is advantageous for multi-sample imaging. The water-based Sca*l*e and SeeDB methods also have simple protocols, though the resulting sample transparency is insufficient for rapid whole-brain imaging of the adult brain. 3DISCO and CLARITY produce highly transparentized brain samples but require careful handling of reagents or specialized devices. CLARITY also requires expensive clearing reagents such as *FocusClear* for final clearing before imaging. In contrast, CUBIC produced a highly transparent brain specimen at lower cost (Table S1) and using nontoxic water-soluble chemicals. Second, the CUBIC protocol can be used with many different types of fluorescent proteins (Figures 3 and 6) and to compare multiple samples by 3D-IHC (Figure 4). This efficient and highly reproducible method also enabled time-course expression profiling with single-cell resolution. Third, the CUBIC protocol is scalable, as it achieved transparentization of a larger primate brain (Figure 5) while preserving detailed subcellular structures such as the axons and spines of neurons (Figure S5). CUBIC reagents can also be used to clear acrylamide-gel-embedded samples prepared according to the CLARITY protocol (Chung et al., 2013), if necessary (Figure S1C). The CUBIC protocol and reagents have the potential to be modified or optimized based on specific sample or experimental needs. For example, our preliminary tests revealed that it was possible to prepare partially cleared samples for two-photon microscopy by using a low-stringency version of reagent 1 for several hours.

Rapid whole-brain imaging cannot deliver its maximum benefit without imaging devices optimized for the cleared tissues. Because LSFM showed potential for high-performance whole-brain imaging early in its development (Dodt et al., 2007), we optimized LSFM for lower spherical aberration (Figure S3A) and acquired 25 whole-brain images, most of which were collected within a few days. Our optimized LSFM setup could capture seamless whole-brain images with relatively high resolution. This is particularly important for comparing multiple 3D whole-brain images with single-cell resolution because the assembly of numerous plane images still has issues such as unavoidable errors of mechanical stage accuracy, the need for additional calculations to correct for optical distortion and rotation for reconstitution, or the accumulation of huge data sets (Emmenlauer et al., 2009; Preibisch et al., 2009). Improvements in illumination (Kalchmair et al., 2010; Leischner et al., 2009) and image processing (Mertz and Kim, 2010) and technological sharing through open platforms such as OpenSPIM (Pitrone et al., 2013) will also advance the speed and resolution of whole-brain imaging. In addition, the development of an RI-adjusted objective lens will further facilitate the high-resolution imaging of CUBIC samples.

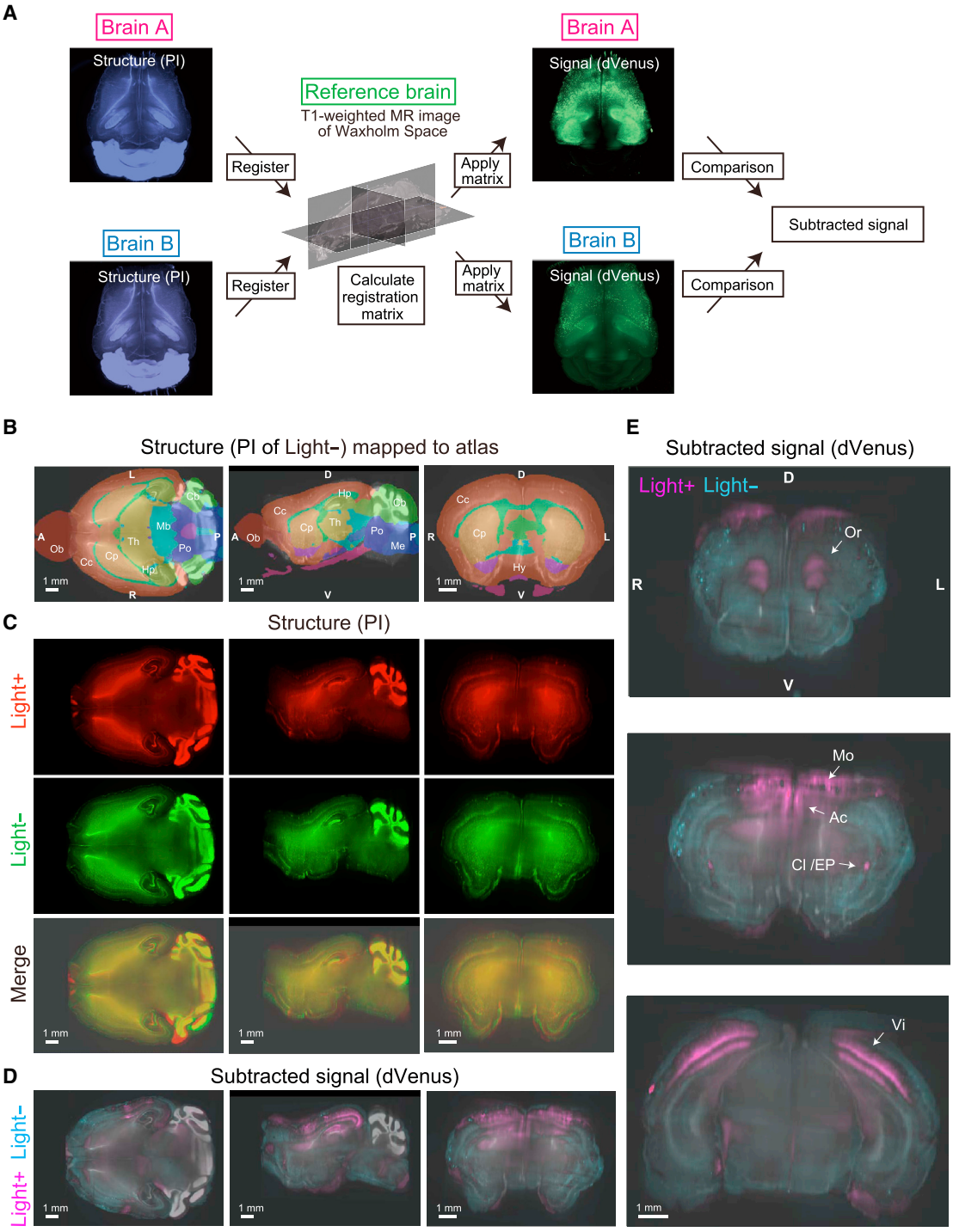

Figure 7. Computational Image Analysis Enables Gene Expression Profiling of Adult Whole Brains

(A) Scheme of CUBIC informatics pipeline (see Figure S7A). Structural information from a nuclear-stained image is used for registration to a reference brain so that a standardization matrix can be calculated. The resulting matrix is then applied to the corresponding signal image. Standardized images from different brains can be merged directly to generate a subtracted signal image.

(B) Standardized PI image mapped to the Waxholm Space atlas, after V-D and D-V image combination and standardization to the reference brain. The analysis was performed using downscaled NIfTI-1 files and visualized with ITK-SNAP (see Extended Experimental Procedures; also in C–E). Ob, olfactory bulb; Cc, cerebral cortex; Cp, caudoputamen; Hp, hippocampus; Th, thalamus; Mb, midbrain; Po, pons; Me, medulla; Cb, cerebellum; Hy, hypothalamus.

(C) PI images of two different brains (Light+ (1), red and Light−, green) and their overlays after V-D and D-V image combination, sample alignment, and standardization to the reference brain.

(legend continued on next page)

CUBIC Enables Whole-Brain Imaging with Single-Cell Resolution

In this study, we conducted whole-brain nuclear counterstaining using SYTO 16 or PI and successfully acquired structural information with anatomical annotation, which is important for whole-brain imaging with single-cell resolution (Figures 6B, 6C, and 7). Because CUBIC preserves global anatomical structure in brain specimens, the anatomical annotation was highly reproducible; for example, the PI images of two different brains in Light+ and Light− mice show substantial overlap (Figure 7C). In addition, the computationally standardized PI image mapped well to a "reference" brain such as that in the Waxholm Space atlas (Figure 7B), enabling reliable annotation of the observed signals. Imaging can be further improved by combining two whole-brain images of the same brain captured from opposite directions (D-V and V-D). Using an edge detection algorithm, it was possible to automatically define a weighted sum between images from these two directions and obtain a combined image that was sharp throughout the brain (Figures 7 and S7). This improved both the alignment to the reference structures and the clarity of the fluorescent signal images. The CUBIC protocol, together with CUBIC informatics, enabled the accurate comparison of multiple whole-brain images. This high-throughput method enables efficient handling of a large number of brain samples. This is particularly useful when investigating dynamic biological phenomena.

To realize system-level identification and analysis of cellular circuits in the brain, it will be important to combine high-throughput whole-brain imaging with other key technologies. One interesting synergy may exist with CRISPR/Cas-mediated genetically engineered mice, in which knockin animals harboring neural-activity reporters (e.g., Arc-dVenus) can be generated within a single generation (Yang et al., 2013). The comprehensive description of phenotype-correlated cells using such knockin mice is an important step in determining the cellular circuits underlying biological phenomena of interest. If neural activity modifiers such as tetanus toxin (Yamamoto et al., 2003), Allatostatin (Tan et al., 2006), or DREADDs and PSAMs (Armbruster et al., 2007; Magnus et al., 2011) could be selectively introduced and expressed in a limited population of cells together with a fluorescent protein marker, phenotype-responsive cells could be functionally identified by whole-brain imaging. The combination of neural activity modifiers (expressed in a limited neural population) and neural activity reporters (expressed throughout the brain) with CUBIC could enable the identification and analysis of functional connectivity at the whole-brain level. In addition, anterograde and retrograde neural tracers, when used with the CUBIC protocol, could also provide direct connectivity information at the whole-brain level (Wickersham et al., 2007). When combined with other emerging technologies, CUBIC should contribute to the system-level identification and analysis of cellular circuits in the whole brain and probably in the whole body. New research fields such as whole-brain cell profiling or whole-body cell profiling (WBC profiling) lie ahead.

EXPERIMENTAL PROCEDURES

See Extended Experimental Procedures for additional details.

The CUBIC Protocol

Sca*l*eCUBIC-1 (reagent 1) was prepared as a mixture of 25 wt% urea (Nacalai Tesque Inc., 35904-45, Japan), 25 wt% *N,N,N′,N′*-tetrakis(2-hydroxypropyl) ethylenediamine (Tokyo Chemical Industry CO., LTD., T0781, Japan), and 15 wt% polyethylene glycol mono-*p*-isooctylphenyl ether/Triton X-100 (Nacalai Tesque Inc., 25987-85, Japan). Sca*l*eCUBIC-2 (reagent 2) was prepared as a mixture of 50 wt% sucrose (Nacalai Tesque Inc., 30403-55, Japan), 25 wt% urea, 10 wt% 2,2′,2′′-nitrilotriethanol (Wako Pure Chemical Industries Ltd., 145-05605, Japan), and 0.1% (v/v) Triton X-100. For whole-brain clearing, each fixed brain was immersed in 10 g of reagent 1 at 37°C with gentle shaking for 3 days, after which the solution was exchanged and the sample immersed in the same volume of fresh reagent 1 for an additional 3–4 days. The treated brain was washed with PBS several times at room temperature while gently shaking, immersed in 20% (w/v) sucrose in PBS, degassed, and immersed in reagent 2 (10 g per brain) for 3–7 days. After imaging, the sample was again washed with PBS, immersed in 20% (w/v) sucrose in PBS, and stored in O.C.T. compound at –80°C.

Microscopy

Whole-brain fluorescence images were acquired with an LSFM (Ultramicroscope, LaVision BioTec, Germany) using 488 and 588 nm lasers, an sCMOS camera, and a macrozoom microscope (Figure S3A). Each plane was illuminated from both the right and left sides of the sample, and a merged image was saved. Immunostained SCN and cerebral cortex images were acquired with an inverted confocal microscope (Leica TCS SP8 or Carl Zeiss LSM700). Images of Arc-dVenus Tg brains (Figure S6A) were captured with a fluorescence stereomicroscope using the same settings as previously described (Eguchi and Yamaguchi, 2009). Two-photon imaging was performed using an upright multiphoton microscope (Olympus FV1000, BX61WI or Carl Zeiss LSM7MP).

Image Data Processing and the CUBIC Informatics

All raw imaging data were collected in a lossless TIFF format. 3D-rendered images were visualized and captured with Imaris software (Version 7.6.4, Bitplane). 3D brain images in the NIfTI-1 format are constructed with Convert3D from ITK-SNAP (Yushkevich et al., 2006). The combination of two images acquired from opposite directions into a single composite 3D image ensured the optimal sharpness of the 3D brain images. The reference atlas used in our analysis was the Waxholm Space Atlas (Johnson et al., 2010). To facilitate analysis across samples, whole-brain images were registered and aligned to reference structures. We aligned images by pairs, in which one image corresponded to the structural information (obtained via nuclear staining) and the other to the fluorescent signal channel. Thus, the analysis of each pair required two steps: (1) registration of the structural information to a reference and (2) alignment of both images by applying the transformation (calculated during registration) to both the structural image and the fluorescent image (Figure 7A). For image registration, we used advanced normalization tools (ANTs), which have proved successful in resolving a number of image registration issues (Murphy et al., 2011).

(D) Subtraction data of Light+ (1) and Light− dVenus images, corresponding to sections in (B) and (C).
(E) Subtraction data of Light+ (1) and Light− dVenus images, corresponding to coronal images in Figures 6B and 6C. Pink and light blue indicate regions where the Venus signals were stronger under Light+ and Light− conditions, respectively. Areas where Venus signals were increased in the Light+ brain are indicated as in Figure 6B. In (D) and (E), images were overlaid with the PI data of Light+ (1) specimen.
See also Figure S7.

SUPPLEMENTAL INFORMATION

Supplemental Information includes Extended Experimental Procedures, seven figures, one table, and seven movies and can be found with this article online at http://dx.doi.org/10.1016/j.cell.2014.03.042.

AUTHOR CONTRIBUTIONS

H.R.U., E.A.S., K.T., and D.P. designed the study. E.A.S. performed most of the biological experiments. K.T. performed chemical screening. D.P. performed most of the computational image analysis. F.K. contributed to the chemical screening. T.T. and H.Y. contributed to the computational image analysis. T.M.W. settled the LSFM imaging system. C.Y. and H.O. housed marmosets and prepared marmoset brains. M.E. and S.Y. prepared Arc-dVenus brains. T.A. and H.K. produced R26-H2B-mCherry and -EGFP mice. Y.S. produced recombinant fluorescent proteins. A.M. provided details on previous brain-clearing methods. All authors discussed the results and commented on the manuscript text.

ACKNOWLEDGMENTS

We thank the lab members at RIKEN CDB and QBiC, in particular, S. Hirahara, J. Hara, H. Ukai, N. Koide, J. Yoshida, C. Imai, and Y. Niwa for their kind help in preparing the materials and C. Jolley for helpful advice. We also thank T. Imai for sharing the SeeDB protocol before its publication, H. Hama for testing Sca*l*e protocol with our samples before its publication, H. Niwa for providing a vector with a CAG promoter, H. Sekiya for supporting two-photon imaging experiments, the LARGE, RIKEN CDB for housing the mice, Emi Kosano for illustrating the mouse in Figure 6, and Olympus and Olympus Engineering for optimizing the Ultramicroscope setup. This work was supported by the Program for Innovative Cell Biology by Innovative Technology from the Ministry of Education, Culture, Sports, Science and Technology (MEXT) of Japan, a Grant-in-Aid for Scientific Research (S) (Grant No. 25221004) and a Grant-in-Aid for Scientific Research on Innovative Areas (Grant No. 23115006) from MEXT/Japan Society for the Promotion of Science (JSPS), the strategic programs for R&D (President's discretionary fund) of RIKEN, an intramural Grant-in-Aid from the RIKEN Center for Developmental Biology and RIKEN Quantitative Biology Center, a grant from Core Research for Evolutional Science and Technology (CREST) and Precursory Research for Embryonic Science and Technology (PRESTO) of Japan Science and Technology Agency (JST), the RIKEN Special Postdoctoral Research Program, a Grant-in-Aid from Japan Foundation for Applied Enzymology, a Grant-in-Aid from the Shimabara Science Promotion Foundation, and by the RIKEN Foreign Postdoctoral Researcher Program.

Received: January 20, 2014
Revised: March 3, 2014
Accepted: March 27, 2014
Published: April 17, 2014

REFERENCES

Abe, T., Kiyonari, H., Shioi, G., Inoue, K.I., Nakao, K., Aizawa, S., and Fujimori, T. (2011). Establishment of conditional reporter mouse lines at ROSA26 locus for live cell imaging. Genesis *49*, 579–590.

Abrahamson, E.E., and Moore, R.Y. (2001). Suprachiasmatic nucleus in the mouse: retinal innervation, intrinsic organization and efferent projections. Brain Res. *916*, 172–191.

Armbruster, B.N., Li, X., Pausch, M.H., Herlitze, S., and Roth, B.L. (2007). Evolving the lock to fit the key to create a family of G protein-coupled receptors potently activated by an inert ligand. Proc. Natl. Acad. Sci. USA *104*, 5163–5168.

Avants, B.B., Tustison, N.J., Song, G., Cook, P.A., Klein, A., and Gee, J.C. (2011). A reproducible evaluation of ANTs similarity metric performance in brain image registration. Neuroimage *54*, 2033–2044.

Becker, K., Jährling, N., Saghafi, S., Weiler, R., and Dodt, H.U. (2012). Chemical clearing and dehydration of GFP expressing mouse brains. PLoS ONE *7*, e33916.

Chudakov, D.M., Matz, M.V., Lukyanov, S., and Lukyanov, K.A. (2010). Fluorescent proteins and their applications in imaging living cells and tissues. Physiol. Rev. *90*, 1103–1163.

Chung, K., Wallace, J., Kim, S.Y., Kalyanasundaram, S., Andalman, A.S., Davidson, T.J., Mirzabekov, J.J., Zalocusky, K.A., Mattis, J., Denisin, A.K., et al. (2013). Structural and molecular interrogation of intact biological systems. Nature *497*, 332–337.

Cormack, A.M. (1973). Reconstruction of densities from their projections, with applications in radiological physics. Phys. Med. Biol. *18*, 195–207.

Dodt, H.U., Leischner, U., Schierloh, A., Jährling, N., Mauch, C.P., Deininger, K., Deussing, J.M., Eder, M., Zieglgänsberger, W., and Becker, K. (2007). Ultramicroscopy: three-dimensional visualization of neuronal networks in the whole mouse brain. Nat. Methods *4*, 331–336.

Eguchi, M., and Yamaguchi, S. (2009). *In vivo* and *in vitro* visualization of gene expression dynamics over extensive areas of the brain. Neuroimage *44*, 1274–1283.

Emmenlauer, M., Ronneberger, O., Ponti, A., Schwarb, P., Griffa, A., Filippi, A., Nitschke, R., Driever, W., and Burkhardt, H. (2009). XuvTools: free, fast and reliable stitching of large 3D datasets. J. Microsc. *233*, 42–60.

Ertürk, A., Becker, K., Jährling, N., Mauch, C.P., Hojer, C.D., Egen, J.G., Hellal, F., Bradke, F., Sheng, M., and Dodt, H.U. (2012). Three-dimensional imaging of solvent-cleared organs using 3DISCO. Nat. Protoc. *7*, 1983–1995.

Feng, G.P., Mellor, R.H., Bernstein, M., Keller-Peck, C., Nguyen, Q.T., Wallace, M., Nerbonne, J.M., Lichtman, J.W., and Sanes, J.R. (2000). Imaging neuronal subsets in transgenic mice expressing multiple spectral variants of GFP. Neuron *28*, 41–51.

Gong, H., Zeng, S.Q., Yan, C., Lv, X.H., Yang, Z.Q., Xu, T.H., Feng, Z., Ding, W.X., Qi, X.L., Li, A.A., et al. (2013). Continuously tracing brain-wide long-distance axonal projections in mice at a one-micron voxel resolution. Neuroimage *74*, 87–98.

Hägerling, R., Pollmann, C., Andreas, M., Schmidt, C., Nurmi, H., Adams, R.H., Alitalo, K., Andresen, V., Schulte-Merker, S., and Kiefer, F. (2013). A novel multistep mechanism for initial lymphangiogenesis in mouse embryos based on ultramicroscopy. EMBO J. *32*, 629–644.

Hama, H., Kurokawa, H., Kawano, H., Ando, R., Shimogori, T., Noda, H., Fukami, K., Sakaue-Sawano, A., and Miyawaki, A. (2011). Sca*l*e: a chemical approach for fluorescence imaging and reconstruction of transparent mouse brain. Nat. Neurosci. *14*, 1481–1488.

Johnson, G.A., Badea, A., Brandenburg, J., Cofer, G., Fubara, B., Liu, S., and Nissanov, J. (2010). Waxholm space: an image-based reference for coordinating mouse brain research. Neuroimage *53*, 365–372.

Kalchmair, S., Jährling, N., Becker, K., and Dodt, H.U. (2010). Image contrast enhancement in confocal ultramicroscopy. Opt. Lett. *35*, 79–81.

Ke, M.T., Fujimoto, S., and Imai, T. (2013). SeeDB: a simple and morphology-preserving optical clearing agent for neuronal circuit reconstruction. Nat. Neurosci. *16*, 1154–1161.

Kitano, H. (2002). Systems biology: a brief overview. Science *295*, 1662–1664.

Kneen, M., Farinas, J., Li, Y.X., and Verkman, A.S. (1998). Green fluorescent protein as a noninvasive intracellular pH indicator. Biophys. J. *74*, 1591–1599.

Land, H., Schütz, G., Schmale, H., and Richter, D. (1982). Nucleotide sequence of cloned cDNA encoding bovine arginine vasopressin-neurophysin II precursor. Nature *295*, 299–303.

Lauterbur, P.C. (1973). Image formation by induced local interactions: Examples employing nuclear magnetic resonance. Nature *242*, 190–191.

Leischner, U., Zieglgänsberger, W., and Dodt, H.U. (2009). Resolution of ultramicroscopy and field of view analysis. PLoS ONE *4*, e5785.

Li, A.A., Gong, H., Zhang, B., Wang, Q.D., Yan, C., Wu, J.P., Liu, Q.A., Zeng, S.Q., and Luo, Q.M. (2010). Micro-optical sectioning tomography to obtain a high-resolution atlas of the mouse brain. Science *330*, 1404–1408.

Magnus, C.J., Lee, P.H., Atasoy, D., Su, H.H., Looger, L.L., and Sternson, S.M. (2011). Chemical and genetic engineering of selective ion channel-ligand interactions. Science *333*, 1292–1296.

Mertz, J., and Kim, J. (2010). Scanning light-sheet microscopy in the whole mouse brain with HiLo background rejection. J. Biomed. Opt. *15*, 016027.

Miller, M.W., and Vogt, B.A. (1984). Direct connections of rat visual cortex with sensory, motor, and association cortices. J. Comp. Neurol. *226*, 184–202.

Murphy, K., van Ginneken, B., Reinhardt, J.M., Kabus, S., Ding, K., Deng, X., Cao, K., Du, K., Christensen, G.E., Garcia, V., et al. (2011). Evaluation of registration methods on thoracic CT: the EMPIRE10 challenge. IEEE Trans. Med. Imaging *30*, 1901–1920.

Navone, F., Greengard, P., and De Camilli, P. (1984). Synapsin I in nerve terminals: selective association with small synaptic vesicles. Science *226*, 1209–1211.

Niwa, H., Yamamura, K., and Miyazaki, J. (1991). Efficient selection for high-expression transfectants with a novel eukaryotic vector. Gene *108*, 193–199.

Ogawa, S., Lee, T.M., Nayak, A.S., and Glynn, P. (1990). Oxygenation-sensitive contrast in magnetic resonance image of rodent brain at high magnetic fields. Magn. Reson. Med. *14*, 68–78.

Pitrone, P.G., Schindelin, J., Stuyvenberg, L., Preibisch, S., Weber, M., Eliceiri, K.W., Huisken, J., and Tomancak, P. (2013). OpenSPIM: an open-access light-sheet microscopy platform. Nat. Methods *10*, 598–599.

Preibisch, S., Saalfeld, S., and Tomancak, P. (2009). Globally optimal stitching of tiled 3D microscopic image acquisitions. Bioinformatics *25*, 1463–1465.

Reep, R.L., Corwin, J.V., and King, V. (1996). Neuronal connections of orbital cortex in rats: topography of cortical and thalamic afferents. Exp. Brain Res. *111*, 215–232.

Sasaki, E., Suemizu, H., Shimada, A., Hanazawa, K., Oiwa, R., Kamioka, M., Tomioka, I., Sotomaru, Y., Hirakawa, R., Eto, T., et al. (2009). Generation of transgenic non-human primates with germline transmission. Nature *459*, 523–527.

Sloniewski, P., Usunoff, K.G., and Pilgrim, C. (1986). Retrograde transport of fluorescent tracers reveals extensive ipsi- and contralateral claustrocortical connections in the rat. J. Comp. Neurol. *246*, 467–477.

Tan, E.M., Yamaguchi, Y., Horwitz, G.D., Gosgnach, S., Lein, E.S., Goulding, M., Albright, T.D., and Callaway, E.M. (2006). Selective and quickly reversible inactivation of mammalian neurons in vivo using the Drosophila allatostatin receptor. Neuron *51*, 157–170.

Tomer, R., Khairy, K., and Keller, P.J. (2011). Shedding light on the system: studying embryonic development with light sheet microscopy. Curr. Opin. Genet. Dev. *21*, 558–565.

van der Horst, G.T.J., Muijtjens, M., Kobayashi, K., Takano, R., Kanno, S., Takao, M., de Wit, J., Verkerk, A., Eker, A.P.M., van Leenen, D., et al. (1999). Mammalian Cry1 and Cry2 are essential for maintenance of circadian rhythms. Nature *398*, 627–630.

Wickersham, I.R., Finke, S., Conzelmann, K.K., and Callaway, E.M. (2007). Retrograde neuronal tracing with a deletion-mutant rabies virus. Nat. Methods *4*, 47–49.

Yamamoto, M., Wada, N., Kitabatake, Y., Watanabe, D., Anzai, M., Yokoyama, M., Teranishi, Y., and Nakanishi, S. (2003). Reversible suppression of glutamatergic neurotransmission of cerebellar granule cells *in vivo* by genetically manipulated expression of tetanus neurotoxin light chain. J. Neurosci. *23*, 6759–6767.

Yang, H., Wang, H.Y., Shivalila, C.S., Cheng, A.W., Shi, L.Y., and Jaenisch, R. (2013). One-step generation of mice carrying reporter and conditional alleles by CRISPR/Cas-mediated genome engineering. Cell *154*, 1370–1379.

Yushkevich, P.A., Piven, J., Hazlett, H.C., Smith, R.G., Ho, S., Gee, J.C., and Gerig, G. (2006). User-guided 3D active contour segmentation of anatomical structures: significantly improved efficiency and reliability. Neuroimage *31*, 1116–1128.